ACS NANO
Cite This: ACS Nano 2019, 13, 11665−11675
www.acsnano.org

ARTICLE

Multiple Anionic Transition-Metal Oxycarbide for Better Lithium Storage and Facilitated Multielectron Reactions

Jing Cuan,[†] You Zhou,[⊥] Jian Zhang,[#] Tengfei Zhou,[†,∥] Gemeng Liang,[†] Sean Li,[▽] Xuebin Yu,[*,§] Wei Kong Pang,[†] and Zaiping Guo[*,†,‡]

[†]Institute for Superconducting and Electronic Materials and [‡]School of Mechanical, Materials and Mechatronics Engineering, University of Wollongong, Wollongong 2511, NSW, Australia

[§]Department of Materials Science, Fudan University, Shanghai 200433, China

[⊥]Faculty of Materials Science and Chemical Engineering, Ningbo University, Ningbo 315211, China

[#]College of Automotive and Mechanical Engineering, Changsha University of Science and Technology, Changsha 410015, China

[∥]College of Chemistry and Materials Science, South-Central University for Nationalities, Wuhan 430074, China

[▽]School of Materials Science and Engineering, University of New South Wales, Sydney 2052, Australia

Supporting Information

ABSTRACT: As an important class of multielectron reaction materials, the applications of transition-metal oxides (TMOs) are impeded by volume expansion and poor electrochemical activity. To address these intrinsic limitations, the renewal of TMOs inspires research on incorporating an advanced interface layer with multiple anionic characteristics, which may add functionality to support properties inaccessible to a single-anion TMO electrode. Herein, a transition-metal oxycarbide (TMOC, M = Mo) with more than one anionic species was prepared as an interface layer on a corresponding oxide. A multiple anionic TMOC possesses advantages of structural stability, abundant active sites, and elevated metal cation valence states. Such merits mitigate volume changes and enhance multielectron reactions significantly. The TMOC nanocomposite has a well-maintained capacity after 1000 cycles at 2 $A \cdot g^{-1}$ and fully resumed rate performance. *In situ* synchrotron X-ray powder diffraction (SXRPD) analysis unveils negligible volume expansions occurring upon oxycarbide layer coupling, with lattice spacing variation less than 1% during cycling. The lithium storage mechanism is further inspected by combined analysis of kinetics, SXRPD, and first-principles calculations. Superior to TMO, multielectron reactions of the TMOC electrode have been boosted due to easier rupture of the metal−oxygen bond. Such improvements underscore the importance of incorporating an oxycarbide configuration as a strategy to expand applications of TMOs.

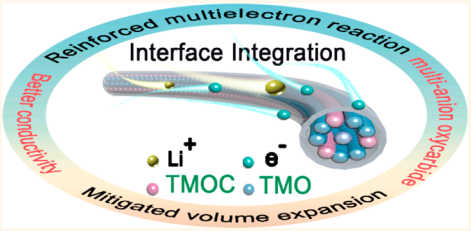

KEYWORDS: *oxycarbide configurations, anion-centered chemistry, multielectron reactions, interface integrations, lithium ion batteries*

With global demands to the large-scale implementation of sustainable energies/smart grids and use of (hybrid) electric vehicles, rechargeable battery technologies, especially lithium ion batteries (LIBs), have experienced rapid development in the last decades.[1−4] To achieve long-term market penetration and satisfy requirements for ever-growing quantities of energy storage, improving the energy density of LIBs places high demands on electrodes that feature the convenient accommodation of electrons and ions at substantial speeds and in substantial amounts.[5−8] The capacitor-like properties and high theoretical capacity of multielectron reaction materials match well with this target, making them eligible candidates for advanced electrode materials of high-performance LIBs.[9]

Transition metal oxides (TMOs) have been viewed as an attractive class of multielectron reaction materials due to their high theoretical capacity, easy functionality, and good safety.[10,11] However, the way in which TMOs could be widely used in high-energy-density battery techniques still remain challenging, since ubiquitous drawbacks in low charge/mass transport capability and large volume changes often give rise to low round-trip efficiency, electrode pulverization, and deteriorating electrochemical performances.[10,12] Furthermore, the feasible multielectron conversion reactions of TMOs require easy rupture of metal−oxygen (M−O) bonds.[13] As the

Received: July 16, 2019
Accepted: September 11, 2019
Published: September 11, 2019

DOI: 10.1021/acsnano.9b05580
ACS Nano 2019, 13, 11665−11675

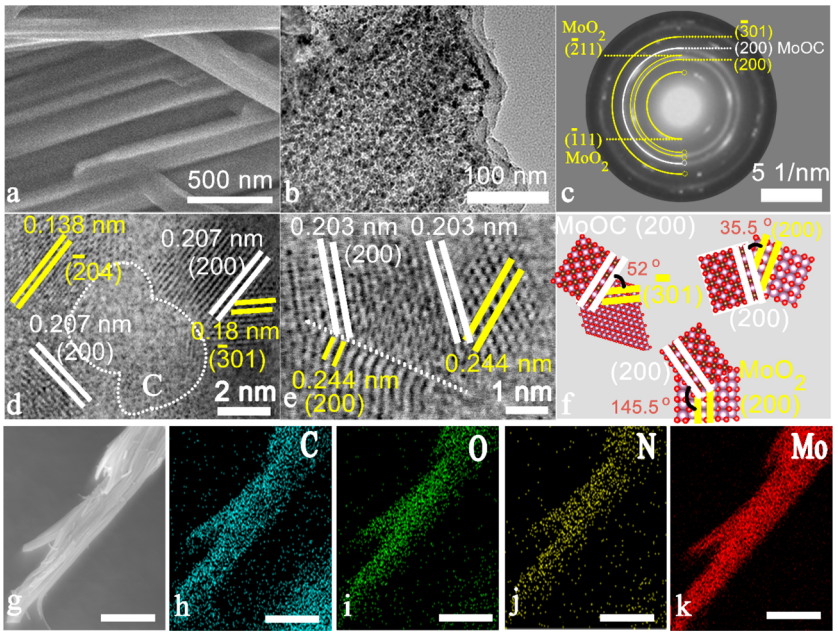

Figure 1. Investigation of the morphological properties of MoOC/MoO_2-NCNW. (a) SEM image of MoOC/MoO_2-NCNW. (b) TEM image of MoOC/MoO_2-NCNW. (c) Selected area electron diffraction (SAED) pattern of MoOC/MoO_2-NCNW. (d, e) High-resolution TEM images of MoOC/MoO_2-NCNW. Yellow labels represent MoO_2 phase, and white labels represent MoOC phase. (f) Schematic illustration of MoOC/MoO_2 heterointerfaces. (g–k) Energy dispersive spectroscopy (EDS) mapping of MoOC/MoO_2-NCNW. Scale bar = 1 μm.

controllable preparation of TMO electrodes flourished with the development of nanotechnology, many strategies have been proposed to solve these issues. Among these strategies, versatile heterostructures combining the merits of each component are encouraging.[14−16] Of particular note, several pioneering works revealed that this strategy was effective to enable faster charge transfer in materials.[14,15] For instance, Gong *et al.* found that in Co_3O_4/$BiVO_4$ heterostructures an internal electric field formed around the p−n heterojunction accelerates/enhances the charge transport process and surface reaction kinetics.[14] Walukiewicz *et al.* reported that both the charge transfer and electron mobility are enhanced at CdO/SnTe heterointerfaces.[17] Therefore, heterostructure designs might engineer TMOs with alluring interfacial properties to obtain an internal charge transfer driving force that facilitates ion/electron diffusion. Nevertheless, poor multielectron reaction activity and cycling durability that originate from intrinsic atomic structures (strong M−O bonds) and volume expansions of TMO electrodes require further solutions. Beyond single-oxide anions, transition-metal compounds with multiple anions (TMMAs), such as transition-metal oxysulfides, oxynitrides, and oxycarbides, have shown good chemical stability, diverse chemistry, and excellent electric conductivity, which may add more functions to modulate skeleton stability, atomic structures, and electronic states of TMOs.[18−20] Therefore, it is promising to address all the concerns by making use of a promising composite, which combines TMMAs and TMOs through an ingenious interface engineering.

Transition-metal oxycarbides (TMOCs) are carbon substituted TMOs that are formed after a carbide anion with a more negative charge (−4 charge) is substituted for part of the lattice oxygen (−2 charge) in TMOs.[21] In comparison with its oxide and carbide counterparts, a TMOC possesses several advantages, involving good conductivity and elevated metal cation oxidation valences stemming from more negatively charged carbide anion substitution, *etc.*[22,23] The elevated metal cation valence is highly desirable for multielectron reactions and could enable higher lithium accommodation per unit mass of compounds. Furthermore, the band gap of TMOC is small due to contribution from the carbon 2p states to near-Fermi states.[24] If an elastic TMOC layer could be integrated on the interfaces of the corresponding TMO, it is anticipated that both electric conductivity and structural stability of the TMOs could be enhanced.

Hence, in this work, by taking molybdenum as an example, we did a preliminary examination of the oxycarbide incorporation effects. To the best of our knowledge, this has been rarely explored in battery research. Notably, a facile strategy has been proposed to integrate MoOC species on the interfaces of MoO_2 using a low-temperature carbon substitution method. We inspected the structural evolutions and electrochemical behaviors of molybdenum dioxide upon coupling with molybdenum oxycarbide, through both experiments and theoretical modeling. Inspection of *in-operando* synchrotron X-ray diffraction (XRD) verified that the dominant MoO_2 phase in MoOC/MoO_2 composites exhibited only slight d-spacing variations ($\Delta_{d\bar{1}11}$ < 1%) in the full lithiation/delithiation state, which implies that small volumetric variation occurs during electrochemical reactions. Furthermore, both lithium storage and multielectron reactions of MoO_2 have been reinforced in the as-prepared MoOC/MoO_2 composites, which may benefit from improved electron/ion transport capability and a reduced multielectron reaction barrier stemming from a longer Mo−O bond. This work highlights the potential of oxycarbide incorporation as a useful strategy to boost the multielectron reaction kinetics and cycling stability of conventional TMO electrodes.

RESULTS AND DISCUSSION

MDOC/MoO_2-N-doped carbon nanowires (MoOC/MoO_2-NCNW) were synthesized through a self-amine-reduction

DOI: 10.1021/acsnano.9b05580
ACS Nano 2019, 13, 11665−11675

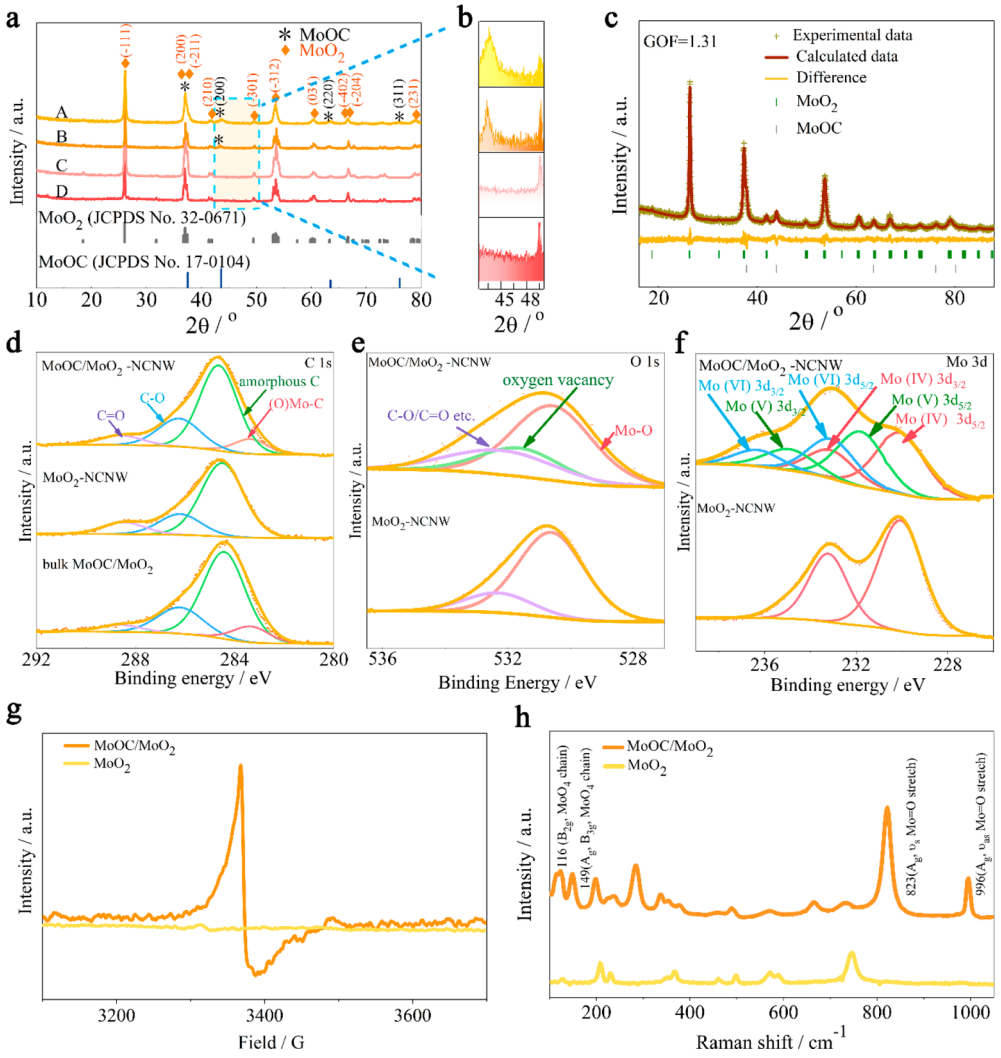

Figure 2. (a) XRD patterns of the as-collected samples: A (MoOC/MoO_2-NCNW), B (bulk MoO_2/MoOC), C (MoO_2-NCNW), and D (bulk MoO_2). (b) XRD patterns of the indicated area in (a). (c) Rietveld refinement analysis of MoOC/MoO_2-NCNW obtained from the XRD data for MoOC/MoO_2-NCNW. (d) C 1s high-resolution XPS spectra of MoOC/MoO_2-NCNW, MoO_2-NCNW, and bulk MoOC/MoO_2. (e) O 1s high-resolution XPS spectra of MoOC/MoO_2-NCNW and MoO_2-NCNW. (f) Mo 3d high-resolution XPS spectra of MoOC/MoO_2-NCNW and MoO_2-NCNW. (g) Electron paramagnetic resonance (EPR) spectra of MoOC/MoO_2-NCNW and MoO_2-NCNW. (h) Raman spectra of MoOC/MoO_2-NCNW and MoO_2-NCNW within the Raman shift of 100−1100 cm^{-1}.

route[25] by mild calcination of $Mo_3O_{10}(C_6H_8N)_2{\cdot}2H_2O$ nanowire templates (monoclinic, *P*21/*(11) phase), which were assembled from infinite chains of $(NH_4)_6Mo_7O_{24}$-aniline coordinating groups, endowing the uniform dispersion of metal species among the carbonaceous units. Samples of MoO_2-NCNW, bulk MoOC/MoO_2, and bulk MoO_2 have also been prepared for comparison (see experimental procedures furnished in the Supporting Information). Field-emission scanning electron microscopy (FESEM) and transmission electron microcopy (TEM) revealed the nanowire-like morphologies of the nanocomposites (MoOC/MoO_2-NCNW, $Mo_3O_{10}(C_6H_8N)_2{\cdot}2H_2O$, MoO_2-NCNW), with a nanowire length of up to several micrometers and a thick sheet-like morphology of the bulk samples (bulk MoOC/MoO_2, bulk MoO_2) (Figure 1 and Figures S1 and S2, Supporting Information). In the panoramic view, the MoOC/MoO_2-NCNW heterocomposite inherits the derivative morphology of $Mo_3O_{10}(C_6H_8N)_2{\cdot}2H_2O$ templates after calcination at a mild inert gas flow rate, and it entails an amorphous carbon layer (~20 nm), manifesting enhanced anchoring of MoO_2/MoOC species on the main carbonaceous matrix. Inspection using selected-area electron diffraction (SAED) patterns (Figure 1c, Figure S2c,f, Supporting Information) demonstrated the finely delineated diffraction rings and polycrystalline nature of the as-synthesized nanocomposite samples. These rings of MoOC/MoO_2-NCNW are associated satisfactorily with the $(\bar{1}11)/(200)/(\bar{3}01)$ crystal planes of MoO_2 phase (JCPDS No. 32-0671) and the (200) crystal planes of second-phase molybdenum oxycarbide (JCPDS No. 17-0104). The sizes of the molybdenum-based particles (MoO_2 and MoOC nanoparticles) in MoOC/MoO_2-NCNW and MoO_2-NCNW samples were identified to be ~3−15 nm. In the clear view of high-resolution TEM images (Figure 1d and e), MoOC/MoO_2-NCNW displays two sets of interplanar distances: one batch pertaining to 0.207 nm are in concordance with the d_{200} spacing of cubic molybdenum oxycarbide, while the other array with spacings of 0.138, 0.18, and 0.244 nm conform with the calculated $d_{\bar{2}04}$, $d_{\bar{3}01}$, and d_{200} values in the XRD pattern of monoclinic MoO_2. In addition, the atomic fringes of MoOC and MoO_2 phases evolved

DOI: 10.1021/acsnano.9b05580
ACS Nano 2019, 13, 11665−11675

smoothly and converged to form heterointerfaces such as $(200)_{MoOC}\|(\bar{3}01)_{MoO2}$ and $(200)_{MoOC}\|(200)_{MoO2}$ (Figure 1e,f). Furthermore, the energy dispersive X-ray spectroscopy elemental mapping images (Figure 1g−k) prove the uniform dispersion of Mo, O, C, and N elements in MoOC/MoO_2-NCNW.

The phase purity and crystallographic structures of the as-prepared samples were investigated by powder XRD analysis (Figure 2a−c and Figure S3, Supporting Information). In Figure 2a,b, patterns A (MoOC/MoO_2-NCNW) and B (bulk MoOC/MoO_2) consist of the typical reflections of monoclinic MoO_2 and additional diffraction peaks (at 43.6°, 63.5°, and 76.3°, marked by stars) that could be assigned to cubic MoOC (JCPDS No. 17-0104), implying the occurrence of successful hybridization between MoO_2 and MoOC phases. On the other hand, all the diffraction peaks in patterns C (MoO_2-NCNW) and D (bulk MoO_2) are exactly attributed to monoclinic MoO_2 (JCPDS No. 32-0671). MoO_2 is extrapolated to be the dominant phase in patterns A−D because of its relatively stronger phase diffraction intensity. No other reflections cam be detected in pattern A or C, indicating the amorphous nature of the carbon matrix.[26,27] As calculated by the Scherrer equation,[28] the Gaussian fitting of the $(200)_{MoOC}$ plane at 2θ = 43.58° (full width at half-maximum (fwhm) of 2.184°) reveals that the average size of MoOC nanoparticles is ∼38.1 Å (3.8 nm), which is consistent with the TEM analysis. Rietveld refinement was performed against the XRD data of MoOC/MoO_2-NCNW to investigate the crystallographic details (Figure 2c). The MoOC crystallizes in a cubic symmetry (with the $Fm\bar{3}m$ space group) with lattice parameters of $a = b = c$ = 4.1587(2) Å, in which Mo occupies the 4*a* sites, C the 4*b* sites, and O the 8*c* sites. On the other hand, monoclinic MoO_2 takes on a distorted rutile structure, where the Mo atom coordinates to six neighboring coordinating oxygen atoms to form a distorted MoO_6 octahedra, which extend along the *c*-axis with edge-sharing connections in the opposite direction.[29] Two sets of alternating Mo−Mo bonds in MoO_2 lead to two types of distinguishable and nonequivalent oxygen coordination sites (O1 and O2, occupying the 4*e* sites) in monoclinic MoO_2. To note, in the rutile structure, only one set of O coordination sites exists, having every oxygen paired by three Mo atoms.[29] The structures and chemical bond distributions, obtained from the refinement analysis, are tabulated in Figure S4 and Tables S1 and S2, Supporting Information. Interestingly, after composing with MoOC, the average Mo−O bond length associated with the MoO_2 phase has lengthened from 2.011 Å to 2.080 Å, indicating an altered bond valence energy landscape in MoO_2. As indicated in previous reports, in the interface model, appropriate truncation of the MoO_6 octahedra that make up the pristine MoO_2 skeleton is promising for tuning the charge states and nucleophilicity of oxygen sites, since the new terminations could involve an atomic rearrangement and lattice distortion toward minimum energy states.[30] As revealed by the crystallographic results, the increased bond length of MoO_2 may stem from strong component interactions after MoOC integration and by which electronically the valence band maximum of MoO_2 is presumably pushed upward due to hybridizations between the MoOC impurity states and MoO_2, bringing forth a narrowed band gap and improved electrical conductivity in the composites. The contents of carbon, MoO_2, and MoOC in MoOC/MoO_2-NCNW and MoO_2-NCNW were calculated by the combined results of Rietveld refinement and thermogravimetric analysis (TGA, Figure S5, Supporting Information), and the results and methods are summarized (Table S3, Supplementary Note 1, Supporting Information).

X-ray photoelectron spectroscopy (XPS) was also conducted over a wide range of bonding energies to further understand these unusual bond configurations and valence bands (Figure 2d−f and Figure S6, Supporting Information). In terms of MoO_2-NCNW, the C 1s peak was deconvolved into three peaks at 284.8, 286.1, and 288.5 eV, which correspond to C−C, C−O, and C═O species in the structure that originates from the decomposition of organic ligands.[31] Compared with this, the new peak of MoOC/MoO_2-NCNW and bulk MoOC/MoO_2 at 283.2 eV has been recognized as C−O−Mo bonds in typical oxycarbide form according to the research by Ledoux *et al.*[32] This agrees well with previous cases such as silicon oxycarbide[33] and aluminum oxycarbide,[34] while it does not conform to the nature of a conventional carbide. This suggests partial C substitution leads to the formation of an oxycarbide intermediate between pure oxide and carbide. In O 1s spectra (Figure 2e and Figure S6b, Supporting Information), peaks due to oxygen vacancies (OVs, 531.7 eV) are evident in MoOC/MoO_2-NCNW and bulk MoOC/MoO_2,[35] with the other two fitted Gaussian peaks at 530.6 and 532.2 eV assigned to Mo−O in the crystal structures and oxygen bonding to C atoms of the carbon matrix (such as C−O/C═O).[36−39] Electron paramagnetic resonance (EPR) tests further confirmed this. An EPR signal at g = 2.071 has been revealed due to unpaired electrons captured by oxygen vacancies in MoOC-modified MoO_2 (Figure 2g).[40,41] Nonetheless, the MoOC-free sample does not display any discernible EPR signal, implying the absence of oxygen vacancies in unmodified MoO_2. The results are consistent with the O 1s XPS analysis, indicating that, on the cleavable surfaces of MoO_2, the intercalation of carbide anions to replace an equal quantity of O sites could reorder the crystal structure, presumably generating considerable oxygen vacancies as thermodynamic entropy increases. In fact, oxygen vacancy as an important family of atomic defects, has a special role in facilitating the charge transfer kinetic and electrochemical activity of the active phase due to its unique shallow donor role, which is able to raise the carrier concentration.[40,42] Hence, the integration of MoOC into the conventional electrode material is highly desirable to achieve such atomic defects and kinetics boosted electrochemical devices. In the Mo 3d XPS spectra (Figure 2f, Figure S6c, Supporting Information), the molybdenum cations have more valence states involving Mo^{6+} and Mo^{5+} configurations in MoOC-MoO_2-NCNW and bulk MoOC/MoO_2.[32] The deconvoluted spectra possess $3d_{3/2}$ peaks at 233.1, 235.0, and 235.9 eV, corresponding to the Mo 3d doublet of Mo^{4+}, Mo^{5+}, and Mo^{6+} triple species, and according to Delporte *et al.*, the Mo^{5+} and Mo^{6+} species mainly originate from MoOC.[32] In accordance with the XPS results, the Raman analysis (Figure 2h,i) demonstrates that the MoOC-containing sample features the typical Mo−O stretching of high molybdenum valence states, with peaks centered at 116, 149, 823, and 996 cm^{-1} assigned to the B_{2g} (along the *c* axis), B_{3g} (along the *b*-direction), A_g mode, and the A_g rigid chains of the terminal Mo−O groups,[36,43] evidencing explicitly the elevated Mo oxidation states of MoOC. In high-valence compounds, high specific capacity is one of the most attractive properties due to the multielectron transfer reactions.[44] Therefore, MoOC is expected to have a higher capacity for Li accommodation. At high Raman modes of carbonaceous MoOC/MoO_2-NCNW

DOI: 10.1021/acsnano.9b05580
ACS Nano 2019, 13, 11665−11675

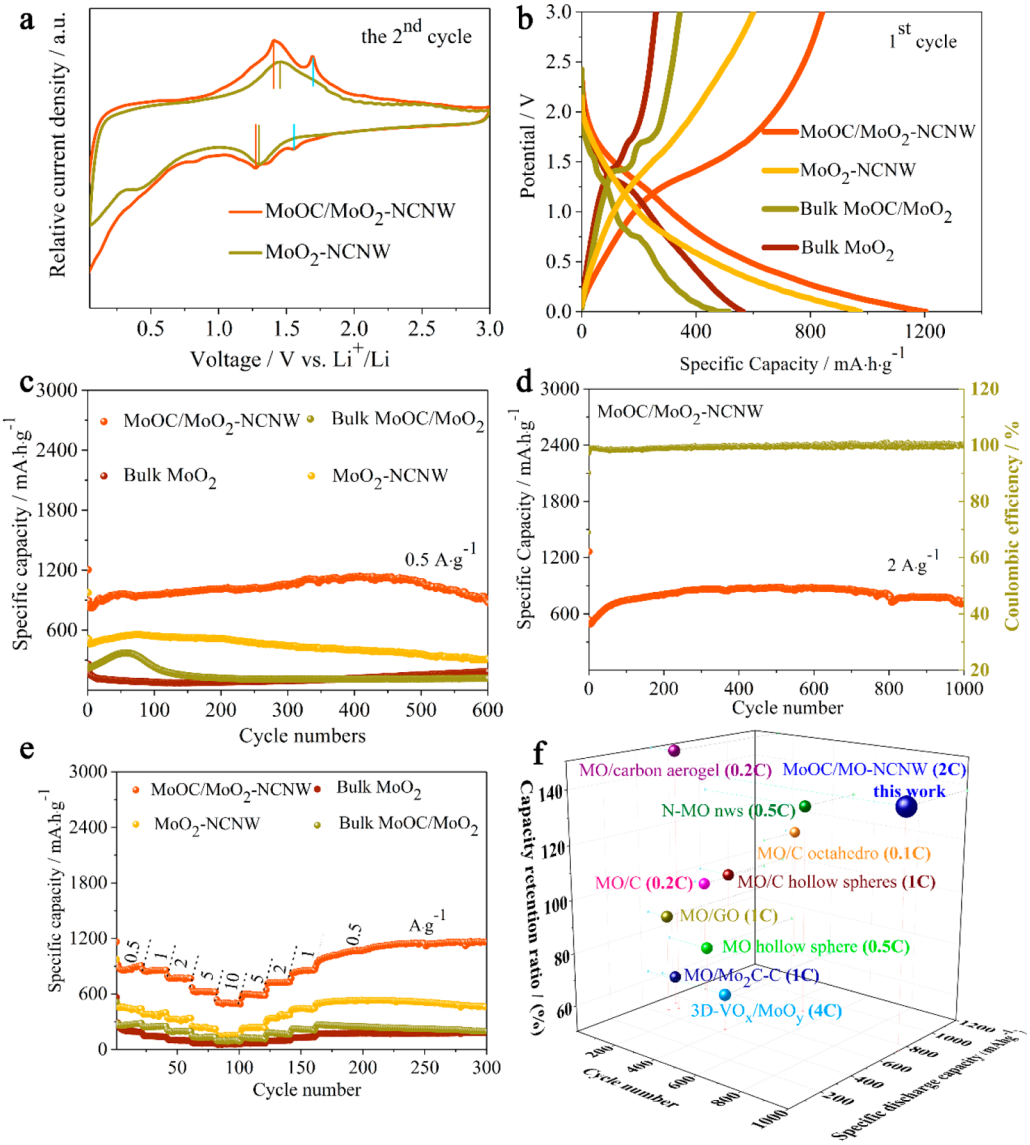

Figure 3. (a) Cyclic voltammetry profiles of MoOC/MoO_2-NCNW and MoO_2-NCNW for the second cycle. (b) Initial charge and discharge profiles of MoOC/MoO_2-NCNW, bulk MoO_2/MoOC, MoO_2-NCNW, and bulk MoO_2 samples at 100 mA·g^{-1}. (c) Long-term galvanostatic cycling comparisons of MoOC/MoO_2-NCNW, bulk MoO_2/MoOC, MoO_2-NCNW, and bulk MoO_2 samples at 0.5 A·g^{-1}. (d) Galvanostatic cycling performance (specific discharge capacity and Coulombic efficiency) of MoOC/MoO_2-NCNW under the current density of 2 A·g^{-1}. (e) Rate performances (specific discharge capacity) of all the samples under the current density of 0.5, 1, 2, 5, 10, 5, 2, 1, and 0.5 A·g^{-1}. (f) State-of-the-art reported molybdenum dioxide (abbreviated as MO)-based electrodes for LIBs.[3650−58]

and MoO_2-NCNW (Figure S7, Supporting Information), the broadband spectrum from 1200 to 1600 cm^{-1} signifies the disorder-induced phonon mode of the D band (at ∼1340 cm^{-1}, sp^3-hybridized carbon atom) overlapping an in-plane graphitic G band (at around 1590 cm^{-1}, in-plane vibration of sp^2-hybridized carbon atoms), which confirms the amorphous carbon coating.[45] The higher intensity ratio of the D to G band (I_D/I_G) in MoOC/MoO_2-NCNW (3.1) than that (∼2.6) of MoO_2-NCNW manifests that more lattice edges or defects exist in the amorphous carbon structure in the MoOC/MoO_2-NCNW composite.[46]

The evolved cyclic voltammograms (CVs) (Figure 3a and Figure S8, Supporting Information) portray multiple redox pairs during Li^+ intecalation/deinterclation into (from) these composites. In Figure 3a, aside from the broadband redox peaks (centered at 1.25/1.40 V, signature of MoO_2 redox reactions), there is a new voltage plateau (oxidation peak ∼1.7 V *vs* Li^+/Li) in MoOC/MoO_2-NCNW, while, there is no visible new voltage plateau in MoO_2-NCNW. What is more, this signal is hard to isolate in bulk MoOC-MoO_2 due to the perturbation from highly crystallized MoO_2 (Figure S8, Supporting Information), since the reduction peaks at 1.27 and 1.56 V are associated with Li^+ intercalation into MoO_2 to form a Li_xMoO_2 phase, while the oxidation peaks at 1.39 and l.69 V are assigned to Li extraction reactions.[47] From the results of this work and Kim *et al.*,[48] the new voltage platform presumably belongs to MoOC, which may entail a conversion reaction similar to that in its counterpart MoO_2. Interestingly, as illustrated in the CV plots, MoOC integration could reduce the overpotentials between redox pairs, which is beneficial to improve the reversibility of conventional MoO_2. This may relate to an enhanced solid-state Li-diffusion process and more facilitated electron transfer, probably due to the presence of rich interfaces in the MoOC-containing composite. It has been

DOI: 10.1021/acsnano.9b05580
ACS Nano 2019, 13, 11665−11675

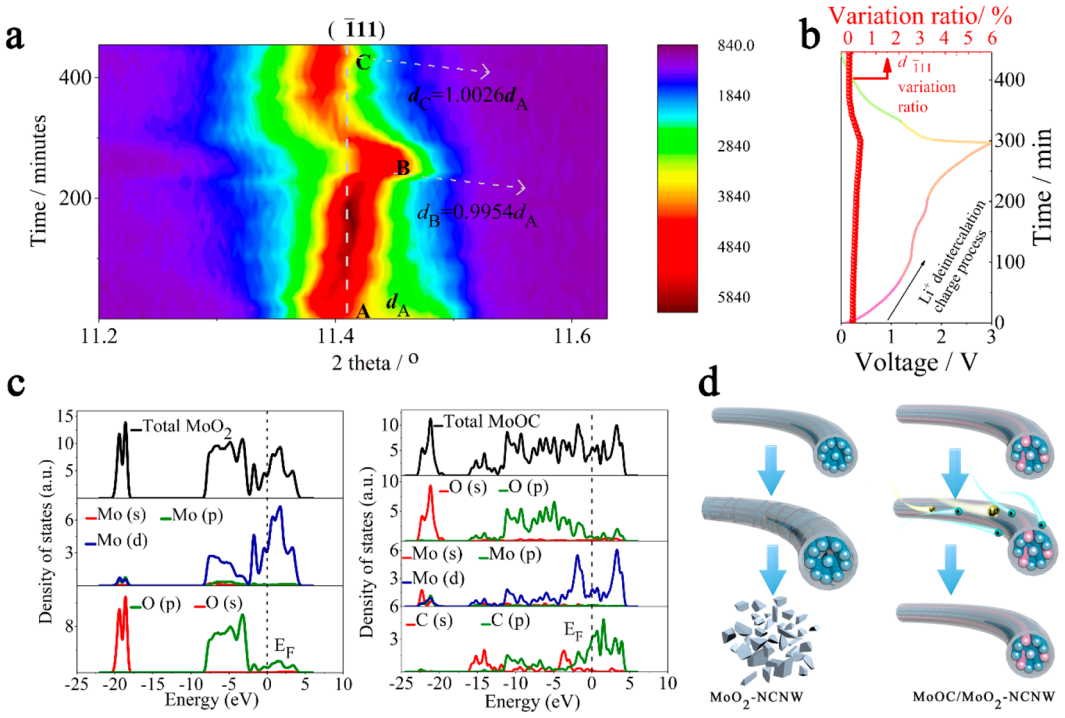

Figure 4. (a) Contour plots using *operando* synchrotron X-ray powder diffraction data of bulk MoOC/MoO_2 composites, collected during electrochemical cycling, showing the variation of the most sensitive ($\bar{1}11$) reflections of the MoO_2 component. (b) Variations of $d_{\bar{1}11}$ in the MoO_2 phase calculated from the ($\bar{1}11$) reflections in (a). (c) Total density of states (TDOS) and partial density of states (PDOS) profiles for pristine MoO_2 (left frame) and MoOC (right frame). (d) Estimated lithium storage mechanisms responsible for the different electrochemical performances of MoO_2-NCNW and MoOC/MoO_2-NCNW. Blue balls: MoO_2. Red balls: MoOC.

reported that abundant interfaces and good electric contact have an important role in maintaining the short diffusion distances inside nanoelectrodes; thereby swifter mass transport could be achieved in the redox reactions of electrodes containing substantial interfaces, as well as improved reversibility.

In the basic galvanostatic discharge−charge (GDC) measurements under 100 mA·g^{-1} (Figure 3b), the MoOC/MoO_2-NCNW electrode shows a first-cycle discharge capacity of 1204 mA·h·g^{-1} with an initial Coulombic efficiency (ICE) of 69.9%. The irreversible capacity of the as-collected electrodes may mainly originate from the formation of a solid-electrolyte interphase and possible side reactions of the cell components.[11,49] MoO_2-NCNW, bulk MoOC/MoO_2, and bulk MoO_2 afford discharge capacities of 974, 514, and 564 mA·h·g^{-1}, with an initial CE of 61.7%, 66.8%, and 46.1%, respectively. As revealed, the higher values of the ICEs in the MoOC-containing group further demonstrate that the redox reactions corresponding to initial lithium storage have been enhanced. To evaluate the long-term discharging/charging durability, the cells were activated under 0.1 A·g^{-1} in the first cycle. MoOC/MoO_2-NCNW delivered a reversible capacity of ∼860 mA·h·g^{-1} after 600 cycles in the prolonged cycling at 0.5 A·g^{-1} (Figure 3c), higher than that of MoO_2-NCNW. Bulk MoOC/MoO_2 shows a higher discharge capacity than bulk MoO_2 in the first 100 cycles, although from 200 cycles, the capacities of both bulk composites are basically flat. In the initial several tens of cycles, the only obvious capacity increase was observed in the MoOC-containing group, showing that Li^+ insertion/removal is more swift in MoO_2 after composing with MoOC.

To assess the cycling durability at high current, MoOC/MoO_2-NCNW was subjected to long-term cycling under the current density of 2 A·g^{-1}, showing a reversible capacity of ∼730 mA·h·g^{-1} even after 1000 cycles, and the capacity increased in the initial cycles (Figure 3d). In testing the rate performances (Figure 3e), the MoOC/MoO_2-NCNW electrode delivered average discharge capacities of ∼860, 844, 752, 617, 480, 581, 710, and 832 mA·h·g^{-1} at current densities of 0.5, 1, 2, 5, 10, 5, 2, and 1 A·g^{-1}, respectively. After the current density has been switched back to 0.5 A·g^{-1}, the specific capacity can fully resume with a moderate capacity increase, attaining ∼1120 mA·h·g^{-1} after 300 cycles. Generally, the capacity retention becomes better in the composite with MoOC. To the best of our knowledge, the electrochemical performance of MoOC/MoO_2-NCNW outperforms many previously reported MoO_2 electrodes (Figure 3f).[36,50−58]

To understand the kinetic aspects of electron transfer and Li^+ diffusion, combined electrochemical impedance spectroscopy (EIS) (Figure S9, Supporting Information) and the galvanostatic intermittent titration technique (GITT) (Figure S10, Supporting Information) measurements were performed. EIS results after 100 cycles imply that the charge transfer resistance falls in the order MoOC/MoO_2-NCNW < MoO_2-NCNW < bulk MoOC/MoO_2 < bulk MoO_2, indicating that the charge transfer kinetics and exchange current density of dominant MoO_2 could be improved after coupling with MoOC.[59] Furthermore, the GITT profiles (Figure S10, Supporting Information) show that the calculated lithium diffusion coefficients (D_{Li^+}) vary between 10^{-12} and 10^{-13} m^2·s^{-1} for bulk MoO_2, while the other three samples have higher D_{Li^+} at around 10^{-11} m^2·s^{-1}. In particular, bulk MoOC/MoO_2 has a comparable Li diffusion capability to MoO_2-NCNW, which confirms the ease of cation (Li^+) movement in MoOC-modified MoO_2. The enhancements in the exchange current

DOI: 10.1021/acsnano.9b05580
ACS Nano 2019, 13, 11665−11675

density and electron/ion transfer, to a great extent, are likely to be responsible for the disparity in the rate performance of MoOC-containing and MoOC-free MoO_2 composites, in consideration that the solid-state Li^+ diffusion (rate-determining step) is one of the most decisive factors among others.[13]

To trace the lithiation/delithiation details of MoO_2 chemistry after hybridizing with MoOC, the structural evolution of the dominant MoO_2 phase was investigated using *in-operando* synchrotron X-ray powder diffraction (λ = 0.688 273 Å) (Figure 4a and Figure S11, Supporting Information). The tested range (from 11° to 19°) could well cover the diffraction peaks of the MoO_2 and MoOC phases. Figure 4a,b show the evolved structure of the MoO_2 main phase. The $(\bar{1}11)$ Bragg diffraction peak of MoO_2 was analyzed, since it is most sensitive to the Li^+ uptake/removal process.[60] It should be noted that the peaks related to the $(\bar{1}11)$ planes of MoO_2 shift toward higher angles under continuous charging. In a complete cycle, the $(\bar{1}11)$ reflection presents a small zigzag migration from 11.42° (point A, fully discharged state) $\xrightarrow[\text{charging}]{}$ 11.46° (point B, monoclinic MoO_2, fully charged state) $\xrightarrow[\text{discharging}]{}$ 11.40° (point C, fully discharged state), signifying the continuous lattice shrinking and enlargement during charging and subsequent discharging.[61] More specifically, as seen from the two-dimensional (2D) colorful contour diagram, the peak for the $(\bar{1}11)$ planes exists over a full cell cycle, showing only varied diffraction intensity without any discovery of new peaks or peak splitting. This suggests the occurrence of a topotactical solid solution transition of MoO_2 (gradual lithiation), which has been often reported in MoO_2-based LIB anodes.[62,63] In another point, the detection angle, $2\theta_{(\bar{1}11)}$ (11.46°, wavelength of 0.688 273 Å, determined using a LaB6 NIST SRM 660b), of modified MoO_2 is slightly smaller than that (11.55°) of unmodified conventional MoO_2, suggesting the enlarged $d_{\bar{1}11}$ spacing of MoO_2 upon coupling with MoOC.[64] The values of $d_{\bar{1}11}$ decrease/increase concomitantly as the charging/discharging proceeds, and as noted in Figure 4b, while its variation ratio was confined to less than 1%. In most previous reports on MoO_2-based materials, the values of lattice spacing show obvious changes.[62,63] The volume evolution of the active phase has a dependence on the migration of lattice planes, so that the minor changes in lattice spacing of the MoOC/MoO_2 heterocomposite suggest its small volumetric changes during electrochemical reactions,[65] and benefiting from this, the electrode structure could be well retained during electrochemical cycling.[66] In addition, *ex situ* TEM results (after 100 cycles) (Figure S12, Supporting Information) confirm that iterative lithium ion extraction/reinsertion does not significantly disrupt the structural integrity of MoOC/MoO_2-NCNW, in comparison with the gradual collapse of the MoO_2-NCNW structure.

Aside from *in-operando* synchrotron XRD, first-principles calculations based on density functional theory were employed to understand the structure−property relationships and electronic configurations of the MoOC-MoO_2 chemistry. A comparison of the total density of states (DOS) at the Fermi level illustrates that, in the MoOC lattice type ($Fm\bar{3}m$ space group), the conduction band contains a significant hybridization of Mo d and C 2p states, giving rise to a higher DOS (5.69 eV) of MoOC than that (4.10 eV) of MoO_2 at the Fermi level (Figure 4c). In line with quantum theory, it is verified that electrons near the Fermi level make an important contribution to the current under an applied electric field,[67] so that the rich population of electrons near the Fermi level of MoOC could contribute to better electronic conductivity of MoOC in comparison with MoO_2. The MoOC incorporated in the MoOC-MoO_2 composite could provide electron transfer pathways and facilitate electron flow to MoO_2. In this way, the electronic conductivity of the whole composite electrode was improved. More specifically, the partial density of states (PDOS) plots demonstrate that, MoO_2 features O 2p states dominating the valence band and Mo d states dominating at the conduction band maximum,[68] which contains five main sections, with Section I spanning from −22 to −6 eV (dominant O 2p states with significant hybridization with Mo d states), Section II from −6 and −2 eV (dominant O 2p states, minor hybridization of Mo d states), Sections III and IV between −2 eV and the Fermi level (mainly Mo d states, with peaks at *ca.* −1.35 and *ca.* −0.5 eV), and above the Fermi level with distinct peaks at ∼1.75 and 3.41 eV (mainly Mo d states). In comparison, MoOC has a notable broadening of its PDOS plots, showing more dispersive patterns of energy bands. The simulated charge density difference plots of MoOC and MoO_2 (Figure S13, Supporting Information) indicated that MoOC may have stronger electronic polarization than MoO_2, and the unbalanced polarization may induce an effective intraband electronic coupling, as is typically understood, especially at the heterojunctions, where have a high content of defects or lattice edges.[69−73] Concomitantly, previous work reported that MoO_2 is vulnerable to a Jahn−Teller effect owing to the less stable $4d^2$ orbitals of the molybdenum(IV) centers.[67] In view of the favorable thermodynamics, the unstable $4d^2$ orbitals of Mo^{4+} in MoO_2 tend to bring forth a structural adjustment, inducing the 4d levels to split into t_{2g} and e_g states and the prior occupation of t_{2g} orbitals by the two electrons.[68] Under altered crystal field stabilization energy (CFSE) and the Jahn−Teller effect, pristine octahedral (Oh) components that build up MoO_2 are expected to take on tetragonal distortion, resulting in the low symmetry of Oh components and the dissonant structure. On account of this, the atomic coupling between MoOC and MoO_2 presumably induces band gap modifications and increased structural dissonance (involving the variations in dangling Mo−O bonds, electronic states, and pristine planarity) of MoO_2 toward minimum energy states. This allows the rational interpretation of the elongated Mo−O bonds in MoO_2 phase after coupling with oxycarbides, illustrating that the easy Mo−O bond cleavage will make multielectron reactions more feasible. The above analysis has shown oxycarbide integration as a facile strategy to reinforce the electrochemical storage performance of a conventional oxide electrode. In comparison with MoO_2-NCNW, the superior electrochemical performances of MoOC-MoO_2-NCNW may benefit significantly from the accelerated ion/electron movement, facilitated multielectron redox reactions, and mitigated volume changes after coupling with oxycarbide (Figure 4d), which renders the stable high-rate capacity (∼730 $mA{\cdot}h{\cdot}g^{-1}$ at 2 $A{\cdot}g^{-1}$, 1000 cycles) of MoOC-MoO_2-NCNW.

CONCLUSIONS

In summary, an ingeniously designed oxycarbide-oxide electrode is systematically investigated in this work, in terms of its reconfigured crystal and electronic structures, electrochemical behaviors (Li^+/electron transfer capability, lithium storage performance), structural evolutions during full lithiation/delithiation cycles *etc.* The investigations, supported by experiments (*in-operando* synchrotron XRD) and theoreti-

DOI: 10.1021/acsnano.9b05580
ACS Nano 2019, 13, 11665−11675

cal modeling, reveal the elongated bond length of the MoO_2 phase where the Mo−O bond is more cleavable, and a regime where multiple electron reactions from the MoOC/MoO_2 heterostructure become more feasible in the composite. Electronically, this may benefit from a strong interaction of the MoOC impurity states and MoO_2 host valence bands, which drastically induces lattice distortion of the truncated MoO_2 lattices toward more stable energy states, causing modified density of states and intrinsically enhanced electron transport capability of MoO_2. Furthermore, the MoOC-MoO_2 heterocomposite has lower lattice spacing variations ($\Delta_{d\bar{1}11}$ < 1%) during cycling, showing significantly alleviated volume changes. This work sheds some light on handling the ubiquity problems of TMOs in charge transfer, volume expansions, poor electric conductivity *etc.*, through oxycarbide integration. Although the extension of the correlative research based on compounds with multiple anions (involving oxynitride, oxysulfide, the proposed oxycarbide material, *etc.*) remains to be investigated in detail, this work has sketched out a future map for a broad space, which used to be limited yet greatly attractive for charge storage.

METHODS

Synthesis of MoOC/MoO_2-NCNW and Bulk MoOC/MoO_2. A 1 mmol amount of ammonium molybdate and 18 mmol of aniline were dispersed in 20 mL of deionized water at 30 °C, and then dilute hydrochloric acid was added into the above solution and the pH was adjusted until a pale yellow, viscous precipitate emerged. Then, the mixed solution was heated at 50 °C for 3 h until a custard-like precipitate formed. Centrifugal separation of the Mo-nanowire precursor precipitate was conducted at 11000 rpm, and it was washed with ethanol at least three times. The samples were dried in air at 50 °C for 24 h. Finally, MoOC/MoO_2-NCNW and bulk MoOC/MoO_2 were obtained by calcining the precipitate of the Mo-nanowire precursor and ammonium molybdate in individual corundum crucibles at 700 °C for 3 h under slow flowing Ar gas.

Synthesis of MoO_2-NCNW and Bulk MoO_2. A 1 mmol amount of ammonium molybdate and 18 mmol of aniline were dispersed in 20 mL of deionized water at 30 °C, and then dilute hydrochloride acid was added into the above solution and the pH was adjusted until a pale yellow, viscous precipitate emerged. The mixed solution was then heated at 50 °C for 3 h until a custard-like precipitate formed. Centrifugal separation of the precipitate was conducted at 11 000 rpm, and it was washed with ethanol at least three times. The samples were dried in air at 50 °C for 24 h. Finally, MoO_2-NCNW and bulk MoO_2 were obtained by calcining the Mo-nanowire precursor and ammonium molybdate in individual corundum crucibles at 700 °C for 3 h under fast flowing Ar gas.

Materials Characterization. Raman spectra of all the samples were recorded using a JobinYvon HR800 Raman spectrometer. The particle size and morphologies of the as-collected samples were characterized by FESEM (JEOL JSM-7500FA). The scanning transmission electron microscope (STEM, JEOL JEM-ARM200F) was set to 200 kV and employed to investigate the detailed crystal structure and provide energy dispersive spectroscopy (EDS) mapping of the products. XPS plots were recorded on a VG Multilab 2000 (VG Inc.) photoelectron spectrometer employing monochromatic Al Kα radiation under vacuum at 2 × 10^{-6} Pa. Continuous-wave EPR experiments were conducted by a Bruker ELEXSYS E580 spectrometer operating in the X-band (9.4 GHz) mode and equipped with an Oxford CF935 helium flow cryostat with an ITC-5025 temperature controller.

Electrochemical Measurements. CR2032 coin-type cells and Celgard separators were used in all electrochemical performance testing, employing lithium metal as counter/reference electrode. Both the cyclic voltammetry profiles and electrochemical impedance spectra were recorded on a VMP-3 electrochemical workstation using a scan rate of 0.1 mV·s^{-1}. The cells were discharged/charged galvanostatically on a Land CT2001A battery tester at different current densities within the voltage range of 0.05−3.0 V *vs* Li^+/Li. GITT tests were also conducted on this apparatus at room temperature in the voltage range of 0.05−3.0 V. A Bitrode unit was programmed to supply a constant current flux (C/10) for 20 min to the cell followed by standing at open circuit for 120 min. The slurries of the working electrodes were prepared through homogeneously mixing the as-synthesized materials, sodium carboxymethyl cellulose, and Super P according to a weight ratio of 80:10:10. The resultant slurries were pasted on Cu foil, vacuum-dried at 80 °C for 12 h, and then pressed at 300 kg·cm^{-2}. The material mass loading on the individual electrodes was around 1.0 mg·cm^{-2}. The electrolyte consisted of 1 M $LiPF_6$ in ethylene carbonate/diethyl carbonate/dimethyl carbonate (volumetric ratio of 1:1:1).

DFT Calculations. The convergence criteria of relaxation were 2.0 × 10^{-5} Ha, 0.004 Ha/Å, and 0.005 Å for energy, gradient, and atomic displacement, respectively. For the MoOC crystals, the structure was optimized in a cubic cell (space group *Fm*/3*m*) with lattice parameters of a = 4.1587 Å, b = 4.1587 Å, c = 4.1587 Å, and $\alpha = \beta = \gamma = 90°$. For the MoO_2 crystals, the structure was optimized in a monoclinic cell (space group *P*21/*c*) with lattice parameters of a = 5.6289 Å, b = 4.8696 Å, c = 5.6222 Å, $\alpha = \gamma = 90°$, and β = 120.4446°.

ASSOCIATED CONTENT

Supporting Information

The Supporting Information is available free of charge on the ACS Publications website at DOI: 10.1021/acsnano.9b05580.

SEM images, TEM images, XRD pattern, crystal structures, TGA profiles, XPS survey spectra, Raman curves, CV curves, EIS, GITT, *operando* synchrotron X-ray powder diffraction data, TEM images after cycling, and charge distribution simulated based on DFT calculations; tables showing previously reported bond length for MoO_2 and cell parameters for calculated models (PDF)

AUTHOR INFORMATION

Corresponding Authors

*E-mail: yuxuebin@fudan.edu.cn (X. Yu).
*E-mail: zguo@uow.edu.au (Z. Guo).

ORCID

You Zhou: 0000-0003-2482-260X
Tengfei Zhou: 0000-0002-7364-0434
Xuebin Yu: 0000-0002-4035-0991
Wei Kong Pang: 0000-0002-5118-3885
Zaiping Guo: 0000-0003-3464-5301

Notes

The authors declare no competing financial interest.

ACKNOWLEDGMENTS

This work was partially supported by the National Science Fund for Distinguished Young Scholars (Grant No. 51625102), the National Natural Science Foundation of China (Grant Nos. 51471053 and 51802357), the Science and Technology Commission of Shanghai Municipality (Grant No. 17XD1400700), Hubei Provincial Natural Science Foundation of China (2018CFB237), and the Fundamental Research Funds for the Central Universities (CZT19003) and are gratefully acknowledged. Also, financial support provided by the Australian Research Council (ARC) (Grant Nos. LP160101629, DE190100504, and FT150100109) is gratefully acknowledged. The authors thank the Electron Microscopy

DOI: 10.1021/acsnano.9b05580
ACS Nano 2019, 13, 11665−11675

Centre (EMC) at the University of Wollongong. The authors also thank Dr. T. Silver and Dr. J. Knott for critical reading of the manuscript. The authors also thank Dr. Y. Zheng for his help in assembling the batteries for *operando* synchrotron X-ray powder diffraction test. Part of this research was undertaken on the Powder Diffraction beamline at the Australian Synchrotron, Victoria, Australia.

REFERENCES

(1) Guo, Y. G.; Hu, J. S.; Wan, L. J. Nanostructured Materials for Electrochemical Energy Conversion and Storage Devices. *Adv. Mater.* **2008**, *20*, 2878−2887.
(2) Wang, Y.; Yu, X.; Xu, S.; Bai, J.; Xiao, R.; Hu, Y. S.; Li, H.; Yang, X. Q.; Chen, L.; Huang, X. A Zero-Strain Layered Metal Oxide as the Negative Electrode for Long-Life Sodium-Ion Batteries. *Nat. Commun.* **2013**, *4*, 2365.
(3) Lu, J.; Lei, Y.; Lau, K. C.; Luo, X.; Du, P.; Wen, J.; Assary, R. S.; Das, U.; Miller, D. J.; Elam, J. W. A Nanostructured Cathode Architecture for Low Charge Overpotential in Lithium-Oxygen Batteries. *Nat. Commun.* **2013**, *4*, 2383.
(4) Kang, K.; Meng, Y. S.; Bréger, J.; Grey, C. P.; Ceder, G. Electrodes with High Power and High Capacity for Rechargeable Lithium Batteries. *Science* **2006**, *311*, 977−980.
(5) Zhou, H.; Zhu, S.; Hibino, M.; Honma, I.; Ichihara, M. Lithium Storage in Ordered Mesoporous Carbon (CMK-3) with High Reversible Specific Energy Capacity and Good Cycling Performance. *Adv. Mater.* **2003**, *15*, 2107−2111.
(6) Xia, L.; Wang, S.; Liu, G.; Ding, L.; Li, D.; Wang, H.; Qiao, S. Flexible SnO_2/N-Doped Carbon Nanofiber Films as Integrated Electrodes for Lithium-Ion Batteries with Superior Rate Capacity and Long Cycle Life. *Small* **2016**, *12*, 853−859.
(7) Wang, C.; Wu, L.; Wang, H.; Zuo, W.; Li, Y.; Liu, J. Fabrication and Shell Optimization of Synergistic TiO_2-MoO_3 Core-Shell Nanowire Array Anode for High Energy and Power Density Lithium-Ion Batteries. *Adv. Funct. Mater.* **2015**, *25*, 3524−3533.
(8) Wang, S.; Zhang, L.; Sun, C.; Shao, Y.; Wu, Y.; Lv, J.; Hao, X. Gallium Nitride Crystals: Novel Supercapacitor Electrode Materials. *Adv. Mater.* **2016**, *28*, 3768−3776.
(9) Chen, R.; Luo, R.; Huang, Y.; Wu, F.; Li, L. Advanced High Energy Density Secondary Batteries with Multi-Electron Reaction Materials. *Adv. Sci.* **2016**, *3*, 1600051.
(10) Yu, S. H.; Feng, X.; Zhang, N.; Seok, J.; Abruna, H. D. Understanding Conversion-Type Electrodes for Lithium Rechargeable Batteries. *Acc. Chem. Res.* **2018**, *51*, 273−281.
(11) Wang, H.; Cui, L. F.; Yang, Y.; Sanchez Casalongue, H.; Robinson, J. T.; Liang, Y.; Cui, Y.; Dai, H. Mn_3O_4− Graphene Hybrid as a High-Capacity Anode Material for Lithium Ion Batteries. *J. Am. Chem. Soc.* **2010**, *132*, 13978−13980.
(12) Yu, S. H.; Lee, S. H.; Lee, D. J.; Sung, Y. E.; Hyeon, T. Conversion Reaction-Based Oxide Nanomaterials for Lithium Ion Battery Anodes. *Small* **2016**, *12*, 2146−2172.
(13) Hu, X.; Zhang, W.; Liu, X.; Mei, Y.; Huang, Y. Nanostructured Mo-based Electrode Materials for Electrochemical Energy Storage. *Chem. Soc. Rev.* **2015**, *44*, 2376−2404.
(14) Chang, X.; Wang, T.; Zhang, P.; Zhang, J.; Li, A.; Gong, J. Enhanced Surface Reaction Kinetics and Charge Separation of *p-n* Heterojunction Co_3O_4/$BiVO_4$ Photoanodes. *J. Am. Chem. Soc.* **2015**, *137*, 8356−8359.
(15) Mai, L. Q.; Yang, F.; Zhao, Y. L.; Xu, X.; Xu, L.; Luo, Y. Z. Hierarchical $MnMoO_4$/$CoMoO_4$ Heterostructured Nanowires with Enhanced Supercapacitor Performance. *Nat. Commun.* **2011**, *2*, 381.
(16) Zhang, J.; Huang, Y.; Mao, C.; Peng, P. Synergistic Effect of Ti and F Co-Doping on Dehydrogenation Properties of Mgh_2 from First-Principles Calculations. *J. Alloys Compd.* **2012**, *538*, 205−211.
(17) Nishitani, J.; Yu, K. M.; Walukiewicz, W. Charge Transfer and Mobility Enhancement at CdO/SnTe Heterointerfaces. *Appl. Phys. Lett.* **2014**, *105*, 132103.
(18) Kageyama, H.; Hayashi, K.; Maeda, K.; Attfield, J. P.; Hiroi, Z.; Rondinelli, J. M.; Poeppelmeier, K. R. Expanding Frontiers in Materials Chemistry and Physics with Multiple Anions. *Nat. Commun.* **2018**, *9*, 772.
(19) Wang, S.; Li, L.; Shao, Y.; Zhang, L.; Li, Y.; Wu, Y.; Hao, X. Transition-metal Oxynitride: A Facile Strategy for Improving Electrochemical Capacitor Storage. *Adv. Mater.* **2019**, *31*, 1806088.
(20) Wang, S.; Shao, Y.; Liu, W.; Wu, Y.; Hao, X. Elastic Sandwich-Type GaN/MnO_2/MnON Composites for Flexible Supercapacitors with High Energy Density. *J. Mater. Chem. A* **2018**, *6*, 13215−13224.
(21) Afir, A.; Achour, M.; Saoula, N. X-ray Diffraction Study of Ti−O−C System at High Temperature and in a Continuous Vacuum. *J. Alloys Compd.* **1999**, *288*, 124−140.
(22) Miller, D. N.; Azad, A. K.; Delpouve, H.; Quazuguel, L.; Zhou, J.; Sinha, A.; Wormald, P.; Irvine, J. T. Studies on the Crystal Structure, Magnetic and Conductivity Properties of Titanium Oxycarbide Solid Solution ($TiO_{1-x}C_x$). *J. Mater. Chem. A* **2016**, *4*, 5730−5736.
(23) Wang, H.; Liu, S.; Smith, K. J. Synthesis and Hydrodeoxygenation Activity of Carbon Supported Molybdenum Carbide and Oxycarbide Catalysts. *Energy Fuels* **2016**, *30*, 6039−6049.
(24) Enyashin, A.; Bamburov, V.; Ivanovskii, A. New Nanotubes of Metal Oxycarbides: Modeling of Carbothermal Reduction of TiO_2 Nanotubes. *Dokl. Phys. Chem.* **2006**, *407*, 57−61.
(25) Gao, Q.; Yang, L.; Lu, X.; Mao, J.; Zhang, Y.; Wu, Y.; Tang, Y. Synthesis, Characterization and Lithium-Storage Performance of MoO_2/Carbon Hybrid Nanowires. *J. Mater. Chem.* **2010**, *20*, 2807−2812.
(26) Yao, X.; Huang, N.; Han, F.; Zhang, Q.; Wan, H.; Mwizerwa, J. P.; Wang, C.; Xu, X. High-Performance All-Solid-State Lithium-Sulfur Batteries Enabled by Amorphous Sulfur-Coated Reduced Graphene Oxide Cathodes. *Adv. Energy Mater.* **2017**, *7*, 1602923.
(27) Dong, S.; Chen, X.; Gu, L.; Zhou, X.; Li, L.; Liu, Z.; Han, P.; Xu, H.; Yao, J.; Wang, H. One Dimensional MnO_2/Titanium Nitride Nanotube Coaxial Arrays for High Performance Electrochemical Capacitive Energy Storage. *Energy Environ. Sci.* **2011**, *4*, 3502−3508.
(28) Patterson, A. The Scherrer Formula for X-Ray Particle Size Determination. *Phys. Rev.* **1939**, *56*, 978−982.
(29) de Castro, I. A.; Datta, R. S.; Ou, J. Z.; Castellanos-Gomez, A.; Sriram, S.; Daeneke, T.; Kalantar-Zadeh, K. Molybdenum Oxides - from Fundamentals to Functionality. *Adv. Mater.* **2017**, *29*, 1701619.
(30) Tokarz-Sobieraj, R.; Witko, M. Electronic Properties of the Active Sites Present at the (011) Surface of MoO_2. *Adsorpt. Sci. Technol.* **2007**, *25*, 583−596.
(31) Yuan, S.; Bao, J. L.; Wang, L.; Xia, Y.; Truhlar, D. G.; Wang, Y. Graphene-Supported Nitrogen and Boron Rich Carbon Layer for Improved Performance of Lithium-Sulfur Batteries due to Enhanced Chemisorption of Lithium Polysulfides. *Adv. Energy Mater.* **2016**, *6*, 1501733.
(32) Delporte, P.; Pham-Huu, C.; Vennegues, P.; Ledoux, M. J.; Guille, J. Physical Characterization of Molybdenum Oxycarbide Catalyst; TEM, XRD and XPS. *Catal. Today* **1995**, *23*, 251−267.
(33) Porte, L.; Sartre, A. Evidence for a Silicon Oxycarbide Phase in the Nicalon Silicon Carbide Fibre. *J. Mater. Sci.* **1989**, *24*, 271−275.
(34) Bou, M.; Martin, J.; Le Mogne, T.; Vovelle, L. Chemistry of the Interface between Aluminium and Polyethyleneterephthalate by XPS. *Appl. Surf. Sci.* **1991**, *47*, 149−161.
(35) Tan, H.; Zhao, Z.; Zhu, W.; Coker, E. N.; Li, B.; Zheng, M.; Yu, W.; Fan, H.; Sun, Z. Oxygen Vacancy Enhanced Photocatalytic Activity of Pervoskite $SrTiO_3$. *ACS Appl. Mater. Interfaces* **2014**, *6*, 19184−19190.
(36) Wang, C.; Sun, L.; Zhang, F.; Wang, X.; Sun, Q.; Cheng, Y.; Wang, L. Formation of Mo-Polydopamine Hollow Spheres and Their Conversions to MoO_2/C and Mo_2C/C for Efficient Electrochemical Energy Storage and Catalyst. *Small* **2017**, *13*, 1701246.
(37) Liu, J.; Tang, S.; Lu, Y.; Cai, G.; Liang, S.; Wang, W.; Chen, X. Synthesis of Mo_2N Nanolayer Coated MoO_2 Hollow Nanostructures as High-Performance Anode Materials for Lithium-Ion Batteries. *Energy Environ. Sci.* **2013**, *6*, 2691−2697.

DOI: 10.1021/acsnano.9b05580
ACS Nano 2019, 13, 11665−11675

(38) Xia, F.; Hu, X.; Sun, Y.; Luo, W.; Huang, Y. Layer-by-layer Assembled MoO_2-Graphene Thin Film as A High-Capacity and Binder-Free Anode for Lithium-Ion Batteries. *Nanoscale* **2012**, *4*, 4707−4711.
(39) Sun, Y.; Hu, X.; Luo, W.; Huang, Y. Self-assembled Hierarchical MoO_2/Graphene Nanoarchitectures and Their Application as A High-Performance Anode Material for Lithium-Ion Batteries. *ACS Nano* **2011**, *5*, 7100−7107.
(40) Kim, H. S.; Cook, J. B.; Lin, H.; Ko, J. S.; Tolbert, S. H.; Ozolins, V.; Dunn, B. Oxygen Vacancies Enhance Pseudocapacitive Charge Storage Properties of MoO_{3-x}. *Nat. Mater.* **2017**, *16*, 454−460.
(41) Wang, Z.; Yang, C.; Lin, T.; Yin, H.; Chen, P.; Wan, D.; Xu, F.; Huang, F.; Lin, J.; Xie, X. H-Doped Black Titania with Very High Solar Absorption and Excellent Photocatalysis Enhanced by Localized Surface Plasmon Resonance. *Adv. Funct. Mater.* **2013**, *23*, 5444−5450.
(42) Zheng, J.; Lyu, Y.; Wang, R.; Xie, C.; Zhou, H.; Jiang, S. P.; Wang, S. Crystalline TiO_2 Protective Layer with Graded Oxygen Defects for Efficient and Stable Silicon-Based Photocathode. *Nat. Commun.* **2018**, *9*, 3572.
(43) Dieterle, M.; Weinberg, G.; Mestl, G. Raman Spectroscopy of Molybdenum Oxides. *Phys. Chem. Chem. Phys.* **2002**, *4*, 812−821.
(44) Gao, X. P.; Yang, H. X. Multi-Electron Reaction Materials for High Energy Density Batteries. *Energy Environ. Sci.* **2010**, *3*, 174−189.
(45) Guo, D.; Qin, J.; Yin, Z.; Bai, J.; Sun, Y. K.; Cao, M. Achieving High Mass Loading of $Na_3V_2(PO_4)_3$@ Carbon on Carbon Cloth by Constructing Three-Dimensional Network between Carbon Fibers for Ultralong Cycle-Life and Ultrahigh Rate Sodium-Ion Batteries. *Nano Energy* **2018**, *45*, 136−147.
(46) Geng, J.; Kong, B. S.; Yang, S. B.; Youn, S. C.; Park, S.; Joo, T.; Jung, H. T. Effect of SWNT Defects on the Electron Transfer Properties in P3HT/SWNT Hybrid Materials. *Adv. Funct. Mater.* **2008**, *18*, 2659−2665.
(47) Zhao, X.; Wang, H. E.; Chen, X.; Cao, J.; Zhao, Y.; Garbe Neale, Z.; Cai, W.; Sui, J.; Cao, G. Tubular MoO_2 Organized by 2D Assemblies for Fast and Durable Alkali-Ion Storage. *Energy Storage Materials* **2018**, *11*, 161−169.
(48) Xiu, Z.; Kim, D.; Alfaruqi, M. H.; Song, J.; Kim, S.; Duong, P. T.; Mathew, V.; Baboo, J. P.; Kim, J. Ultrafine Molybdenum Oxycarbide Nanoparticles Embedded in N-Doped Carbon as A Superior Anode Material for Lithium-Ion Batteries. *J. Alloys Compd.* **2017**, *696*, 143−149.
(49) Lee, S. W.; Yabuuchi, N.; Gallant, B. M.; Chen, S.; Kim, B. S.; Hammond, P. T.; Shao-Horn, Y. High-Power Lithium Batteries from Functionalized Carbon-Nanotube Electrodes. *Nat. Nanotechnol.* **2010**, *5*, 531.
(50) Che, Y.; Zhu, X.; Li, J.; Sun, J.; Liu, Y.; Jin, C.; Dong, C. Simple Synthesis of MoO_2/Carbon Aerogel Anodes for High Performance Lithium Ion Batteries from Seaweed Biomass. *RSC Adv.* **2016**, *6*, 106230−106236.
(51) Zeng, L.; Huang, X.; Chen, X.; Zheng, C.; Liu, R.; Chen, G.; Qian, Q.; Chen, Q.; Wei, M. Ethanol Thermal Reduction Synthesis of Hierarchical MoO_2-C Hollow Spheres with High Rate Performance for Lithium Ion Batteries. *RSC Adv.* **2016**, *6*, 105558−105564.
(52) Xia, G.; Liu, D.; Zheng, F.; Yang, Y.; Su, J.; Chen, Q. Preparation of Porous MoO_2@C Nano-Octahedrons from A Polyoxometalate-Based Metal-Organic Framework for Highly Reversible Lithium Storage. *J. Mater. Chem. A* **2016**, *4*, 12434−12441.
(53) Yang, L. C.; Sun, W.; Zhong, Z. W.; Liu, J. W.; Gao, Q. S.; Hu, R. Z.; Zhu, M. Hierarchical MoO_2/N-Doped Carbon Heteronanowires with High Rate and Improved Long-Term Performance for Lithium-Ion Batteries. *J. Power Sources* **2016**, *306*, 78−84.
(54) Zhu, Y.; Wang, S.; Zhong, Y.; Cai, R.; Li, L.; Shao, Z. Facile Synthesis of A MoO_2-Mo_2C-C Composite and Its Application as Favorable Anode Material for Lithium-Ion Batteries. *J. Power Sources* **2016**, *307*, 552−560.
(55) Petnikota, S.; Teo, K. W.; Chen, L.; Sim, A.; Marka, S. K.; Reddy, M. V.; Srikanth, V. V.; Adams, S.; Chowdari, B. V. Exfoliated Graphene Oxide/MoO_2 Composites as Anode Materials in Lithium-Ion Batteries: An Insight Into Intercalation of Li and Conversion Mechanism of MoO_2. *ACS Appl. Mater. Interfaces* **2016**, *8*, 10884−10896.
(56) Zhao, D.; Qin, J.; Zheng, L.; Cao, M. Amorphous Vanadium Oxide/Molybdenum Oxide Hybrid with Three-Dimensional Ordered Hierarchically Porous Structure as a High-Performance Li-Ion Battery Anode. *Chem. Mater.* **2016**, *28*, 4180−4190.
(57) Xiao, D.; Zhang, J.; Li, X.; Zhao, D.; Huang, H.; Huang, J.; Cao, D.; Li, Z.; Niu, C. Nanocarved MoS_2-MoO_2 Hybrids Fabricated Using *In Situ* Grown MoS_2 as Nanomasks. *ACS Nano* **2016**, *10*, 9509−9515.
(58) Wang, Y.; Yu, L.; Lou, X. W. Formation of Triple-Shelled Molybdenum-Polydopamine Hollow Spheres and Their Conversion into MoO_2 /Carbon Composite Hollow Spheres for Lithium-Ion Batteries. *Angew. Chem., Int. Ed.* **2016**, *55*, 14668−14672.
(59) Zhou, G.; Wang, D. W.; Li, L.; Li, N.; Li, F.; Cheng, H. M. Nanosize SnO_2 Confined in the Porous Shells of Carbon Cages for Kinetically Efficient and Long-Term Lithium Storage. *Nanoscale* **2013**, *5*, 1576−1582.
(60) Kumar Sen, U.; Shaligram, A.; Mitra, S. Intercalation Anode Material for Lithium Ion Battery based on Molybdenum Dioxide. *ACS Appl. Mater. Interfaces* **2014**, *6*, 14311−14319.
(61) Wang, S.; Yang, J.; Wu, X.; Li, Y.; Gong, Z.; Wen, W.; Lin, M.; Yang, J.; Yang, Y. Toward High Capacity and Stable Manganese-Spinel Electrode Materials: A Case Study of Ti-Substituted System. *J. Power Sources* **2014**, *245*, 570−578.
(62) Shon, J. K.; Lee, H. S.; Park, G. O.; Yoon, J.; Park, E.; Park, G. S.; Kong, S. S.; Jin, M.; Choi, J. M.; Chang, H.; Doo, S.; Kim, J. M.; Yoon, W. S.; Pak, C.; Kim, H.; Stucky, G. D. Discovery of Abnormal Lithium-Storage Sites in Molybdenum Dioxide Electrodes. *Nat. Commun.* **2016**, *7*, 11049.
(63) Guo, B.; Fang, X.; Li, B.; Shi, Y.; Ouyang, C.; Hu, Y. S.; Wang, Z.; Stucky, G. D.; Chen, L. Synthesis and Lithium Storage Mechanism of Ultrafine MoO_2 Nanorods. *Chem. Mater.* **2012**, *24*, 457−463.
(64) Katsumi, N.; Yonebayashi, K.; Okazaki, M. Evaluation of Stacking Nanostructure in Soil Humic Acids by Analysis of the 002 Band of Their X-Ray Diffraction Profiles. *Soil Sci. Plant Nutr.* **2015**, *61*, 603−612.
(65) Yuan, T.; Tan, Z.; Ma, C.; Yang, J.; Ma, Z. F.; Zheng, S. Challenges of Spinel $Li_4Ti_5O_{12}$ for Lithium-Ion Battery Industrial Applications. *Adv. Energy Mater.* **2017**, *7*, 1601625.
(66) Ohzuku, T.; Ueda, A.; Yamamoto, N. Zero-strain Insertion Material of $Li[Li_{1/3}Ti_{5/3}]O_4$ for Rechargeable Lithium Cells. *J. Electrochem. Soc.* **1995**, *142*, 1431−1435.
(67) Bai, L.; Zhang, Y.; Zhang, L.; Zhang, Y.; Sun, L.; Ji, N.; Li, X.; Si, H.; Zhang, Y.; Huang, H. Jahn-Teller Distortions in Molybdenum Oxides: An Achievement in Exploring High Rate Supercapacitor Applications and Robust Photocatalytic Potential. *Nano Energy* **2018**, *53*, 982−992.
(68) Scanlon, D. O.; Watson, G. W.; Payne, D.; Atkinson, G.; Egdell, R.; Law, D. Theoretical and Experimental Study of the Electronic Structures of MoO_3 and MoO_2. *J. Phys. Chem. C* **2010**, *114*, 4636−4645.
(69) Li, Y.; Zhang, H. R.; Lei, Y.; Chen, Y. Z.; Pryds, N.; Shen, B.; Sun, J. Evidence for Lattice-Polarization-Enhanced Field Effects at the $SrTiO_3$-Based Heterointerface. *Sci. Rep.* **2016**, *6*, 22418.
(70) Zhang, S.; Zheng, Y.; Huang, X.; Hong, J.; Cao, B.; Hao, J.; Fan, Q.; Zhou, T.; Guo, Z. Structural Engineering of Hierarchical Micronanostructured Ge-C Framework by Controlling the Nucleation for Ultralong-life Li Storage. *Adv. Energy Mater.* **2019**, *9*, 1900081.
(71) Zhou, T.; Zheng, Y.; Gao, H.; Min, S.; Li, S.; Liu, H.; Guo, Z. Surface Engineering and Design Strategy for Surface Amorphized TiO_2@Graphene Hybrids for High Power Li-Ion Battery Electrodes. *Adv. Sci.* **2015**, *2*, 1500027.
(72) Liu, Y.; Tai, Z.; Zhou, T.; Sencadas, V.; Zhang, J.; Zhang, L.; Konstantinov, K.; Guo, Z.; Liu, H. An All-Integrated Anode *via* Interlinked Chemical Bonding between Double-Shelled−Yolk-Structured Silicon and Binder for Lithium-Ion Batteries. *Adv. Mater.* **2017**, *29*, 1703028.
(73) Hu, S.; Li, Y.; Chen, Y.; Peng, J.; Zhou, T.; Pang, W. K.; Didier, C.; Peterson, V. K.; Wang, H.; Li, Q.; Guo, Z. Insight of A Phase

DOI: 10.1021/acsnano.9b05580
ACS Nano 2019, 13, 11665−11675

Compatible Surface-Coating for Long-Durable Li-Rich Layered Oxide Cathode. *Adv. Energy Mater.* **2019**, 1901795.

DOI: 10.1021/acsnano.9b05580
ACS Nano 2019, 13, 11665−11675